CLOUD STRUCTURE OF THE NEAREST BROWN DWARFS: SPECTROSCOPIC VARIABILITY OF LUHMAN 16AB FROM THE *HUBBLE SPACE TELESCOPE*

ESTHER BUENZLI[1], DIDIER SAUMON[2], MARK S. MARLEY[3], DÁNIEL APAI[4,5], JACQUELINE RADIGAN[6],
LUIGI R. BEDIN[7], I. NEILL REID[6], AND CAROLINE V. MORLEY[8]
[1] Max Planck Institute for Astronomy, Königstuhl 17, D-69117 Heidelberg, Germany; buenzli@mpia.de
[2] Los Alamos National Laboratory, Mail Stop F663, Los Alamos, NM 87545, USA
[3] NASA Ames Research Center, MS-245-3, Moffett Field, CA 94035, USA
[4] Department of Astronomy, University of Arizona, 933 North Cherry Avenue, Tucson, AZ 85721, USA
[5] Department of Planetary Sciences, University of Arizona, 1629 East University Boulevard, Tucson, AZ 85721, USA
[6] Space Telescope Science Institute, 3700 San Martin Drive, Baltimore, MD 21218, USA
[7] INAF-Osservatorio Astronomico di Padova, Vicolo dell'Osservatorio 5, I-35122 Padova, Italy
[8] Department of Astronomy and Astrophysics, University of California, Santa Cruz, CA 95064, USA

ABSTRACT

The binary brown dwarf WISE J104915.57−531906.1 (also Luhman 16AB), composed of a late-L and early-T dwarf, is a prototypical L/T transition flux reversal binary located at a distance of only 2 pc. Luhman 16B is a known variable whose light curves evolve rapidly. We present a spatially resolved spectroscopic time-series of Luhman 16A and B covering 6.5 hr using the *Hubble Space Telescope*/WFC3 at 1.1–1.66 μm. The small, count-dependent variability of Luhman 16A at the beginning of the observations likely stems from instrumental systematics; Luhman 16A appears non-variable above ≈0.4%. Its spectrum is well fit by a single cloud layer with intermediate cloud thickness ($f_{sed} = 2$, $T_{eff} = 1200$ K). Luhman 16B varies at all wavelengths with peak-to-valley amplitudes of 7%–11%. The amplitude and light curve shape changes over only one rotation period. The lowest relative amplitude is found in the deep water absorption band at 1.4 μm, otherwise it mostly decreases gradually from the blue to the red edge of the spectrum. This is very similar to the other two known highly variable early-T dwarfs. A two-component cloud model accounts for most of the variability, although small deviations are seen in the water absorption band. We fit the mean spectrum and relative amplitudes with a linear combination of two models of a warm, thinner cloud ($T_{eff} = 1300$ K, $f_{sed} = 3$) and a cooler, thicker cloud ($T_{eff} = 1000$–1100 K, $f_{sed} = 1$), assuming out-of-equilibrium atmospheric chemistry. A model with parameters as for Luhman 16A except for the addition of cloud holes cannot reproduce the variability of Luhman 16B, indicating more complex cloud evolution through the L/T transition. The projected separation of the binary has decreased by ≈0″.3 in eight months.

Key words: binaries: visual – brown dwarfs – stars: atmospheres – stars: individual (WISE J104915.57-531906.1, Luhman 16AB) – stars: variables: general

1. INTRODUCTION

The recently discovered brown dwarf binary WISE J104915.57−531906.1 (Luhman 2013), hereafter Luhman 16AB, is one of only a few known spatially resolved binaries where both components are located at the transition of L to T spectral type (L7.5 and T0.5, Kniazev et al. 2013; Burgasser et al. 2013). Its very large parallax of 495 ± 4.6 mas (Boffin et al. 2014) puts it at a distance of only 2.020±0.019 pc, making it the third closest known system from the Sun after α Cen and Barnard's star. Because of that proximity, they are by far the brightest brown dwarfs of their spectral type, allowing studies not previously possible for fainter objects. For example, Crossfield et al. (2014) were able to use time-resolved very high resolution spectroscopy to create a surface map by applying Doppler imaging for the first time to a brown dwarf. The map showed a heterogeneous surface structure for Luhman 16B that may be linked to patchy cloud cover.

Heterogeneous cloud cover has already been inferred for other early-T dwarfs (e.g., Artigau et al. 2009; Radigan et al. 2012; Apai et al. 2013; Radigan et al. 2014) as well as for Luhman 16B (Gillon et al. 2013; Biller et al. 2013; Burgasser et al. 2014) from measurements of photometric and/or spectroscopic variability. The removal of cloud opacity is the dominant driver of the

spectral changes happening between late-L- to mid-T-type dwarfs (e.g., Kirkpatrick 2005; Cushing et al. 2008; Stephens et al. 2009). The change in near-infrared colors from red to blue and the brightening of the *J* band suggest that the clouds, likely composed of silicates and iron, that form opaque layers in late-L dwarfs are fully removed from the visible photosphere by the spectral type of ≈T5 (Dupuy & Liu 2012). These changes happen at nearly constant effective temperatures of $T_{eff} \approx 1300$ K.

One mechanism proposed to explain the color evolution, the re-emergence of the FeH feature from early- to mid-T dwarfs (Burgasser et al. 2002, 2003), and the photometric variability is the appearance and growth of holes in the clouds (Ackerman & Marley 2001; Burgasser et al. 2002; Marley et al. 2010), where flux can then emerge from deeper, hotter regions. Alternatively, cloud thinning through growth of particle size, increased sedimentation efficiency and rapid rain out may also remove the clouds (Tsuji et al. 2004; Knapp et al. 2004; Burrows et al. 2006; Saumon & Marley 2008). The multi-wavelength variability of the two early-T dwarfs 2MASS J21392676+0220226 (hereafter 2M2139) and SIMP J013656.57+093347.3 (hereafter SIMP0136) are not compatible with fully cleared holes in clouds. Instead, models that are a combination of varying covering fraction of thin and thick clouds over one rotation
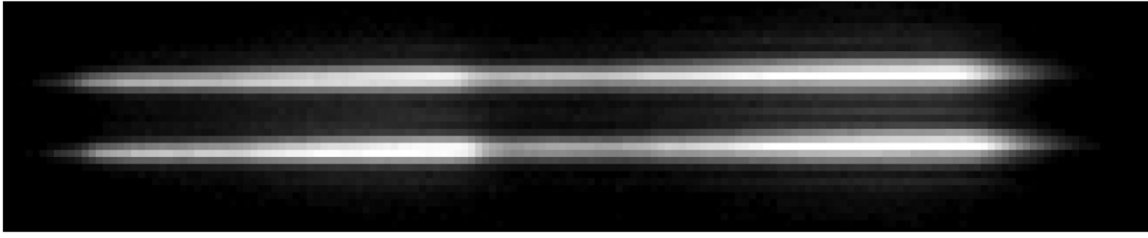
Figure 1. First-order spectra of Luhman 16A (upper) and B (lower) recorded on the detector, spanning from about 1.05 to 1.75 μm. The dispersion direction is approximately toward northeast. The gray scale is logarithmic.

period can reproduce many of the characteristics of the variability (Radigan et al. 2012; Apai et al. 2013; Buenzli et al. 2014).

With Luhman 16B, a third early-T dwarf with multiple percent variability is now available to test whether the two-component thin/thick cloud model can represent the cloud structure at the beginning of the L/T transition. The Luhman 16 system offers many additional benefits to significantly increase our understanding of cloud structure at the L/T transition. Its brightness offers the possibility for studies over a very broad wavelength range, even in the optical (Biller et al. 2013), and a very good signal-to-noise ratio at intermediate (Faherty et al. 2014) or very high resolution (Crossfield et al. 2014). The distance is already known very precisely and the orbital motion will eventually lead to a measurement of the dynamical mass; the orbital timescale is $\approx$25 yr at a separation of $\approx$3 AU. Finally, the A component is most likely co-eval with the B component, implying that their age and metallicity are equal. The A component is brighter overall, but fainter in the *Y* and *J* bands (Burgasser et al. 2013). This flux reversal suggests that cloud evolution has progressed less far than for the B component and it therefore provides a comparison point before the onset of the L/T transition.

Many characteristics of the Luhman 16AB binary have already been constrained. The discovery of lithium in both objects points to an age between 0.1 and 3 Gyr (Faherty et al. 2014). Their masses are therefore in the range of 20–65 M$_J$. From their bolometric luminosities, their effective temperatures are very similar with $T_{\rm eff} = 1310 \pm 30$ K for A and 1280 ± 75 K for B, while the brightness temperature is about 50 K higher for B in regions that are dominated by condensate grain scattering (Faherty et al. 2014). The $v \sin i$ measurements indicate that the inclination of Luhman 16B is <30° from equator-on (Crossfield et al. 2014). The rotation period has been determined as being close to five hours, with formal measurements 4.87 ± 0.01 (Gillon et al. 2013) or 5.05 ± 0.1 hr (Burgasser et al. 2014). Precise determination of the rotation period is difficult because the light curve shape evolves on timescales of only one rotation period.

In this paper, we present spatially resolved spectroscopic time series obtained with the *Hubble Space Telescope* (*HST*) for both Luhman 16A and B. This allows a study of their variability amplitudes independently and with high precision, and gives access to features such as the 1.4 μm water band that are not obtainable from the ground but are important tracers of the vertical extension of the cloud. In Section 2, we describe the observations and data reduction. In Section 3, we present and analyze the measured spectroscopic variability and its evolution over one rotation period. We also provide an update on the binary separation. In Section 4, we model the observations with patchy cloud models and, in Section 5, we discuss and compare to previous results. Our conclusions are presented in Section 6.

2. OBSERVATIONS AND DATA REDUCTION

2.1. Observations

We observed Luhman 16AB on 2013 November 8 between 06:34 and 13:06 (UT) with *HST*/WFC3 in the infrared channel (Program 13280). We observed for five consecutive orbits with gaps in between because the target is hidden behind the Earth for parts of the orbit. The effective observation length per orbit was shortened from a maximum visibility of 57 minutes to 44 minutes because of acquisition and because the maximum number of files that can be stored in the WFC3 buffer is only 304 (counting each non-destructive read). This limit was reached before the end of the target visibility, and the necessary buffer dump took up the rest of the available time per orbit, in which time no further observations can be taken. The gap between the first and second orbit was shorter than between the other orbits because the target is located relatively close to the *HST* continuous viewing zone. In that case, the observations of the target within the first orbit of a multi-orbit visit can be pushed to as late in the visibility as possible to optimize the schedule.

The detector is a Teledyne HgCdTe with a size of 1024×1024 pixels, but we used the 256×256 subarray mode because the full array would allow even fewer observations to be stored before a buffer dump. The pixel size is $\approx$0$\farcs$13, resulting in an field of view of $\approx$30$''$ × 30$''$. At the beginning of each orbit we acquired a direct image through the F132N filter used to measure the location of the sources on the detector for precise wavelength calibration. For the remainder of the orbit, we used the G141 grism to take spectral time series of the binary. The first order of the spectra is fully captured on the subarray, while the zeroth and second orders are not recorded. The spectra have a dispersion of 4.65 nm pixel^{-1} and span $\approx$140 pixels. The orientation of the spacecraft was set to have the line connecting the binary (nearly) perpendicular to the grism dispersion direction to minimize overlap of the two spectra (Figure 1). A number of background objects are also visible in the field, none of which overlap with the brown dwarfs. One is the full first-order spectrum of a fainter background star, several are very faint and are likely higher order spectra of more distant background stars. A zeroth-order image is also visible in the field.

We used the SPARS10 readout mode because the minimum exposure time of the SPARS25 mode, previously successfully for similar observations of brown dwarfs (Buenzli et al. 2012; Apai et al. 2013; Buenzli et al. 2014) would have resulted in saturation of the target. For each exposure, three non-destructive reads of 0 s, 0.278 s and 7.346 s were taken (NSAMP = 2) for a total exposure time of 7.624 s. For the direct images, exposure times were only 0.278 s (NSAMP = 1). The maximum number of counts recorded in an image was $\approx$25,000. This is well below half-well ($\approx$40,000 counts) where image persistence can become relevant. In each orbit, we took 100 exposures with the G141 grism. The cadence (exposure
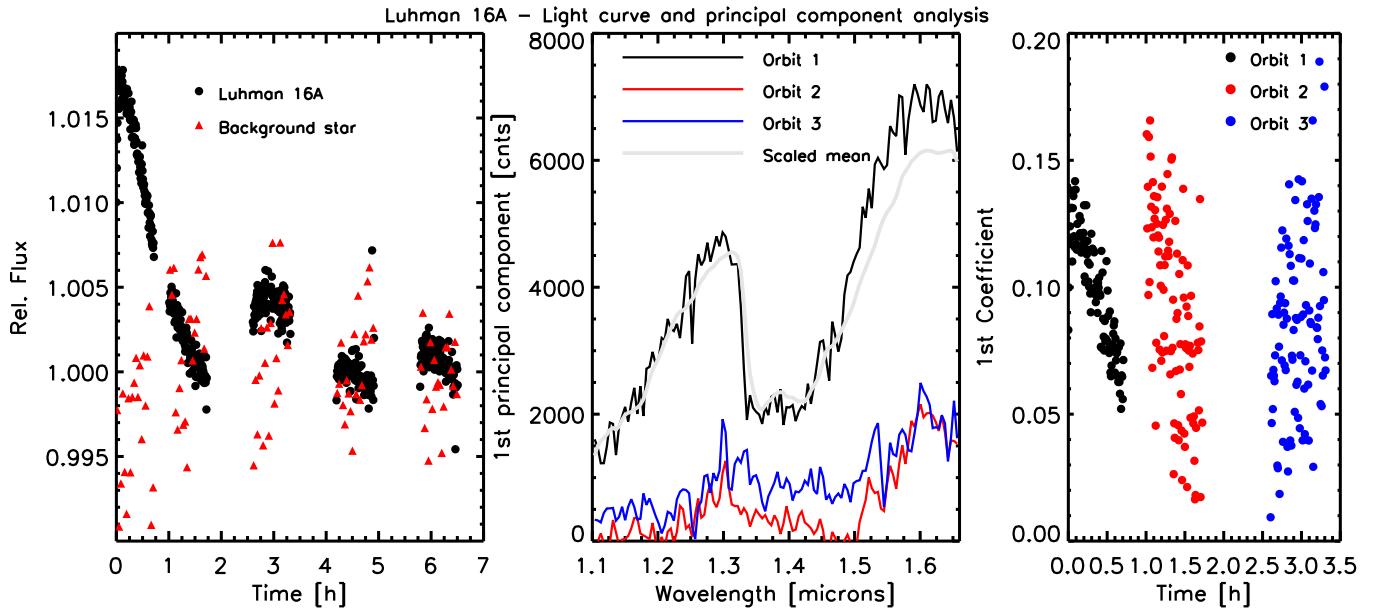
Figure 2. Observations and principal component analysis for Luhman 16A. Left: integrated raw light curve for Luhman 16A (black dots) and a fainter background star (red triangles, binned by factor of five). Middle: first principal component (see the text) derived for orbits 1 (black), 2 (red), and 3 (blue). The average recorded flux in counts (scaled) is shown in gray. The first component for the first orbit appears to be largely proportional to the observed count rate. Right: coefficients corresponding to the first principal component.

time plus overhead) was 26 s, the length of the spectroscopic time series was 43 minutes per orbit spanning a total of 6.5 hr.

We observed in staring mode without dithering to avoid errors from pixel-to-pixel sensitivity variations that cannot be corrected to sufficient precision by flat-fielding.

2.2. Data Reduction

Data reduction was performed using the same method as in Apai et al. (2013) and Buenzli et al. (2014). It is a combination of the standard WFC3 pipeline, custom IDL routines, and the PyRAF software package aXe[9], which is used for extracting and calibrating slitless spectroscopic data.

The WFC3 pipeline `calfw3` outputs `flt` files, which are the combined images from the non-destructive subreads of an exposure. The pipeline subtracted the zero-read and dark current, flagged bad pixels and corrected for nonlinearity and gain. We then identified cosmic rays as $>5\sigma$ outliers for a given pixel compared to the same pixel in the nearest eight frames in the time series and replaced them by the median value of the other frames. To correct flagged bad pixels, we interpolated over nearest neighbors in the same row. We only corrected pixels with flag numbers 4 (dead pixel), 32 (unstable pixel), 256 (saturated), and 512 (bad in flat-field), as the other flagged pixels did not appear to have altered pixel flux above the noise level.

Before running aXe, we embedded the frames into full-frame images and flagged the extra pixels with a data quality flag to exclude them from processing. We first used the `axeprep` routine that subtracts the background by scaling a master sky frame. We then ran the `axecore` routine that flat-fields the frames, performs wavelength calibration, extracts the two-dimensional spectra, and flux-calibrates with the G141 sensitivity curve. We chose the extraction width to be 7 pixels, which includes 88%–92% of the flux of each binary without notable contamination by the other object (see Section 3.1). We applied aperture correction using the values provided by Kuntschner et al. (2011), using

---

9 http://axe-info.stsci.edu

spline interpolation for intermediate wavelengths. We only consider wavelengths between 1.10 and 1.66 μm, outside of these the grism sensitivity drops and the larger errors can negatively impact our subsequent principal component analysis (PCA).

3. RESULTS

The spectral time series reveal variations for Luhman 16B at the several percent level at all wavelengths consistent with earlier variability measurements of this object. They are presented and analyzed in detail in Section 3.2. For Luhman 16A, the strongest variation found is a 1.5% drop in the first two orbits. Our analysis presented in Section 3.1 suggests that this is not intrinsic variability of the brown dwarf but an instrumental systematic. Luhman 16A is most likely non-variable above our noise level of ±0.2%–0.4% level at all covered wavelengths.

3.1. Luhman 16A

The left panel of Figure 2 shows the light curve for Luhman 16A obtained by integrating over the full spectrum. We exclude the few obvious outliers from further analysis. We find a brief sharp increase over the first five exposures and then a strong flux decrease over the first orbit that continues into the second orbit before leveling out. In the third orbit, we find a flux level that is slightly increased by ≈0.5%, and finally a nearly flat curve in the fourth and fifth orbit at the same level as at the end of the second orbit. The shape of the light curve is very different than what would commonly be expected for a rotating brown dwarf with patchy cloud cover and is likely caused by instrumental variations as we demonstrate below.

WFC3 is known to have strong systematics introduced in particular in the first orbit. In previous brown dwarf variability observations, which were all taken with the SPARS25 mode and longer integration time, a ramp with increasing flux level was found (Buenzli et al. 2012; Apai et al. 2013; Buenzli et al. 2014) that appeared to be largely independent of the count rate. However, observations taken in the SPARS10 mode show a

very different behavior that appears to be less stable and shows some indication of a count rate dependence. Transiting planet observations in this mode have revealed a decreasing ramp in the first orbit, though at a lower level than what is measured here (Mandell et al. 2013). In addition, ramps or hooks (continuous or only short flux increase) connected to buffer dumps can be present with strength depending on the array size and number of reads (Swain et al. 2013).

To compare systematic effects we retrieve the light curve of the brightest background star, which is still a factor of $\approx$10–50 fainter than the brown dwarfs, even in their water absorption bands. Contrary to Luhman 16A, we find a slightly increasing ramp in the first orbit (see Figure 2). This supports the strong count rate dependence of this effect, but implies that the background star cannot be used to correct the light curves of the brown dwarfs.

We apply a PCA in order to determine the spectral characteristics of the changes in the first three orbits with respect to the more constant fourth and fifth orbit. We perform the analysis separately for each orbit in order to avoid the first orbit dominating due to the largest changes. During the PCA, instead of subtracting the mean of the full time series or the individual orbit, we subtract the mean of the counts over the fourth and fifth orbit that we consider to be the baseline. For all three orbits, we find that the first component accounts for most of the variations ($>$60% for the first orbit and $\approx$17% for the second and third, where the variations are not much larger than the noise level). The first principal components and their coefficients are shown in Figure 2. The results can be interpreted such that $F(\lambda, t)_{\mathrm{orbit1(2,3)}} \approx <F(\lambda, t)_{\mathrm{orbit4,5}}>_t + a_1(t)e_1(\lambda)$, where $a_1(t)$ is the first coefficient and $e_1(\lambda)$ the first principal component (eigenvector), and $F(\lambda, t)$ the flux measured in counts.

The first principal component of the first orbit reveals that the changes are indeed nearly proportional to the measured count rate, except slightly stronger at wavelengths $>1.5\,\mu$m. In the second orbit, the count rate dependence is less significant but still present, although most of the variation stems from wavelengths $>1.5\,\mu$m. In the third orbit, we also find an increase in the flux peaks in addition to an increasing change with wavelength. The origin of these systematic errors remains unclear. For orbits 2 and 3, there may be some influence from drifts in the Y direction that can lead to the flux being deposited onto regions with slightly different pixel sensitivity. We find small drifts ($\lesssim$0.1 pixels) over the first three orbits, while the position appears to be more stable over orbits 4 and 5. There are also comparable drifts in the X direction that become evident particularly at the boundary of the water absorption feature where the flux drops rapidly and a shift in wavelength direction will have a big impact. This effect is also visible in the second principal component. Because of the limited impact on our conclusions and the strong undersampling of the point-spread function (PSF), we do not attempt to correct for these drifts.

We note that the intrinsic spectral variability of brown dwarfs also shows some correlation with the measured flux, as the largest variations are generally measured in the regions of the highest flux (Apai et al. 2013), while the relative amplitude is lower in the deep water absorption band. However, the relation between measured counts and the counts in the first principal component for Luhman 16B is distinctly different from the single straight line derived for Luhman 16A (Figure 3). Combined with the absence of any evidence for periodicity, the variations of Luhman 16A are therefore unlikely to be astrophysical in
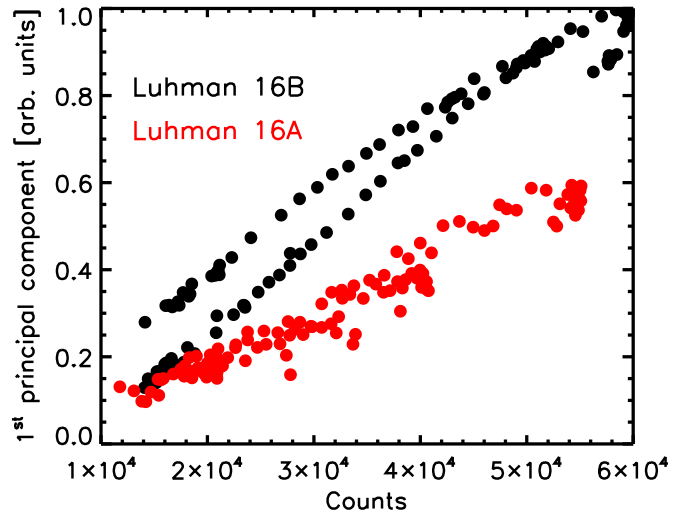

Figure 3. Correlation between the average measured counts and the first principal component of the variability (see the text) for the Luhman 16A (red, first orbit only) compared to Luhman 16B (black). The counts in the first principal component have been scaled arbitrarily.

origin. Nevertheless, we cannot fully exclude that we may have removed small real astrophysical variability for Luhman 16A that is either aperiodic or of considerably longer period than the observations.

In Section 3.1.1 we derive a correction for these errors and conclude that Luhman 16A is most likely non-variable above $\approx$0.2%–0.4% between 1.08 and 1.66 μm.

We also calculate the influence that the small amount of overlapping flux from the B component could have on A. The region extracted for the A component would correspond to flux from B that is located between 7 and 14 pixels away from its peak. According to the aperture correction values of Kuntschner et al. (2011), the amount of flux in this region is 1%–1.5% depending on wavelength. Assuming a relative amplitude of 10% for B (see Section 3.2) implies variations of 0.1%–0.15% for A, which is smaller than our remaining errors.

3.1.1. Correction of Systematic Errors

Because the count rate of Luhman 16B is very comparable to Luhman 16A, the systematics in the first orbit in particular may also have a non-negligible impact on the light curves of Luhman 16B. Here we derive a correction from the PCA of the A component by finding a parameterized form of $a_1(t)e_1(\lambda)$ that is then subtracted from the measured flux $F(\lambda, t)$ for both A and B. For the first three orbits, the parameterization of $a_1(t)$ is determined by a simple linear fit as a function of time (Figure 4, right), where we disregard the first 10 points in the first orbit that form a separate steep rising ramp. For $e_1(\lambda)$, we find a linear fit as a function of the mean number of counts at a given wavelength (Figure 4, middle). While this approach is most valid for the first orbit, to first order it also corrects the much smaller variations in the second and third orbits. For B, we then use this function and interpolate or extrapolate to the measured counts at each wavelength point. In the left panel of Figure 4, we show that after subtracting the parameterized form of $a_1(t)e_1(\lambda)$ from the flux of the A component, the light curve in the first orbit is constant to within $\approx \pm$0.2%. We note that within each orbit there remain small trends, perhaps related to small drifts on the detector, for which we do not correct. The standard deviation over the data set of Luhman 16A as a function of wavelength lies
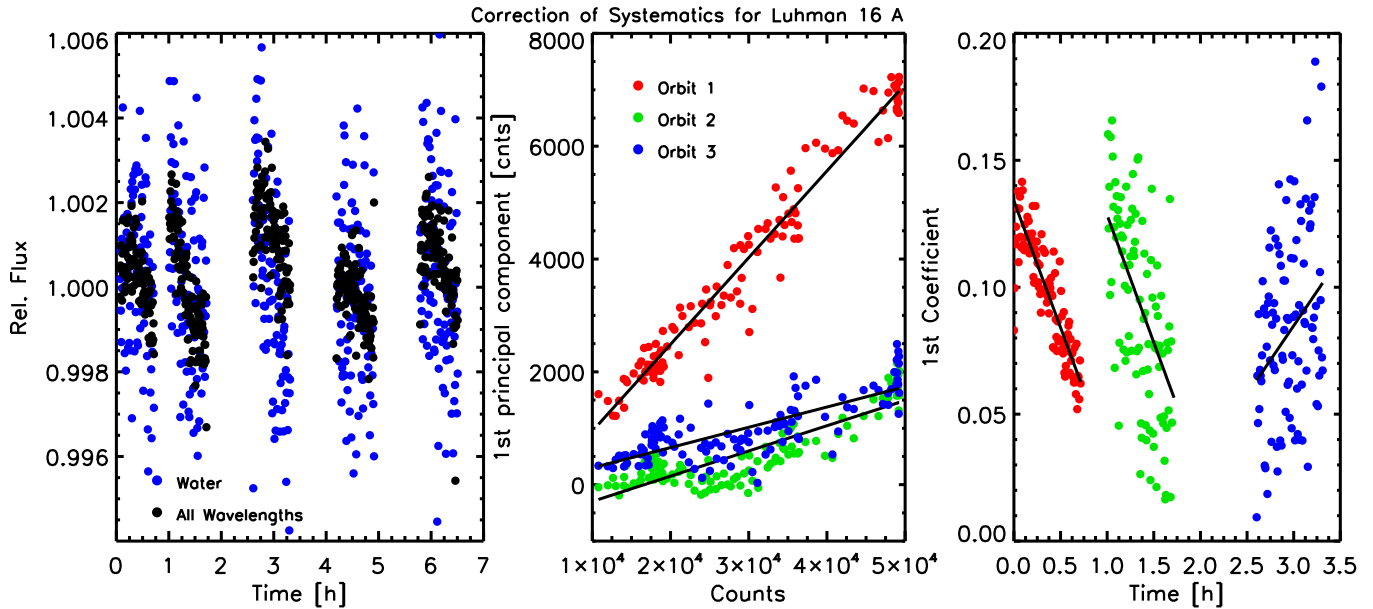
Figure 4. Left: corrected light curve for Luhman 16A integrated over all wavelengths (black dots) and only the water absorption band at 1.35–1.44 μm (blue). Middle: first principal component (see the text) as a function of number of counts of the mean flux at a given wavelength for orbits 1 (red), 2 (green), and 3 (blue) with the best corresponding linear fit (black line). The fitted functions are orbit 1: $-588 + 0.154x$, orbit 2: $-744 + 0.045x$, orbit 3: $-60.5 + 0.036x$. Right: coefficients corresponding to the first principal component with the best corresponding linear fit. The fitted functions are orbit 1: $0.134–0.100x$, orbit 2: $0.229–0.100x$, orbit 3: $-0.078 + 0.054x$.

between 0.2% (flux peaks) and 0.4% (water absorption band and blue edge of the spectrum). This error cannot be assumed to be Gaussian and therefore is not significantly smaller for integrated light curves than for individual wavelength points.

3.2. Luhman 16B

Luhman 16B is variable at all observed wavelengths at a level several times larger than the systematics observed for Luhman 16A (see Section 3.1). We apply the derived instrumental correction (see Section 3.1.1) to the data of Luhman 16B and proceed with the corrected spectra. However, we also performed the subsequent analysis on the uncorrected data for comparison, as well as on data corrected by simply dividing by the normalized raw light curves of Luhman 16A at all wavelengths. The only notable differences lie in the shape of the light curves within the first two orbits. However, the basic conclusions do not depend on whether we correct the instrument systematics or not.

We removed the first five measurements where a steep ramp was found in the data for Luhman 16A, as well as seven points that were strong outliers. We then binned the data to a cadence of 2.14 minutes, typically averaging five observations except where points had been removed.

Figure 5 presents a summary of the observations of Luhman 16B. It shows the maximum and minimum spectrum (each averaged over 3 binned or 15 individual spectra) compared to the mean spectrum of Luhman 16A, as well as the relative amplitude as a function of wavelength, i.e., the difference of the maximum to the minimum spectrum divided by the mean spectrum. This difference has been smoothed with a Gaussian with an FWHM of 2 pixels, which corresponds to one resolution element. Furthermore, the full light curve integrated over different wavelength regions is also shown: the J band and H band peaks and the deep water absorption band at 1.4 μm. For comparison and to give an estimate of the uncertainties, the fully integrated light curve of Luhman 16A is also shown. The light curve shape is not sinusoidal at all wavelengths. We find a rapid steep drop

in the third orbit (9.5%/hr at the steepest location) in the J band. The minimum brightness is likely reached inside the gap shortly after the third orbit. The light curve shows three local maxima with different peak brightnesses: at the end or just after of the first orbit, after the second orbit, and before the fifth orbit, where the overall maximum is likely reached. The peak-to-valley amplitude likely lies between 10%–12% in the J band peak and is about 1% lower in the H band peak and 3.5% lower in the water band. The water band light curve shows small deviations in the shape compared to the J and H peak light curves, these deviations are discussed in more detail in Section 3.2.1.

If the rotation period of Luhman 16B is $\sim$5 h (Gillon et al. 2013; Burgasser et al. 2014), the data in orbits 2 and 5 cover the same rotational phase. However, significant differences are visible in our observations both in the brightness and shape of the light curves. These differences are discussed in more detail in Section 3.2.2.

The wavelength dependence of the relative amplitude shows a gradual decrease from 11% at the blue edge of the spectrum (1.1 μm) to 8% at the red edge, interrupted by a sharp drop to only about 6% at 1.35 μm, where the flux also drops sharply because of a deep water absorption band. The amplitude gradually increases again with a wavelength beyond 1.44 μm to the same level prior to the drop. It is notable that while the absolute variability peaks in the J and H flux peaks, the flux peaks do not correspond to the maximum relative amplitude in the J and H, which is found on the increasing slope blueward of the peak. In the absorption band between 1.1 to 1.18 μm there is also a drop in the ratio, but it is much smaller than in the 1.4 μm band. An interesting effect is seen in the Na I feature at 1.14 μm: even though the flux in this feature is lower than at surrounding wavelengths, the relative amplitude is higher. We do not find comparable anti-correlation in any other absorption feature.

To determine which of the small features in the relative amplitude as a function of wavelength are real, we determine the white noise error per resolution element. Because the flux levels
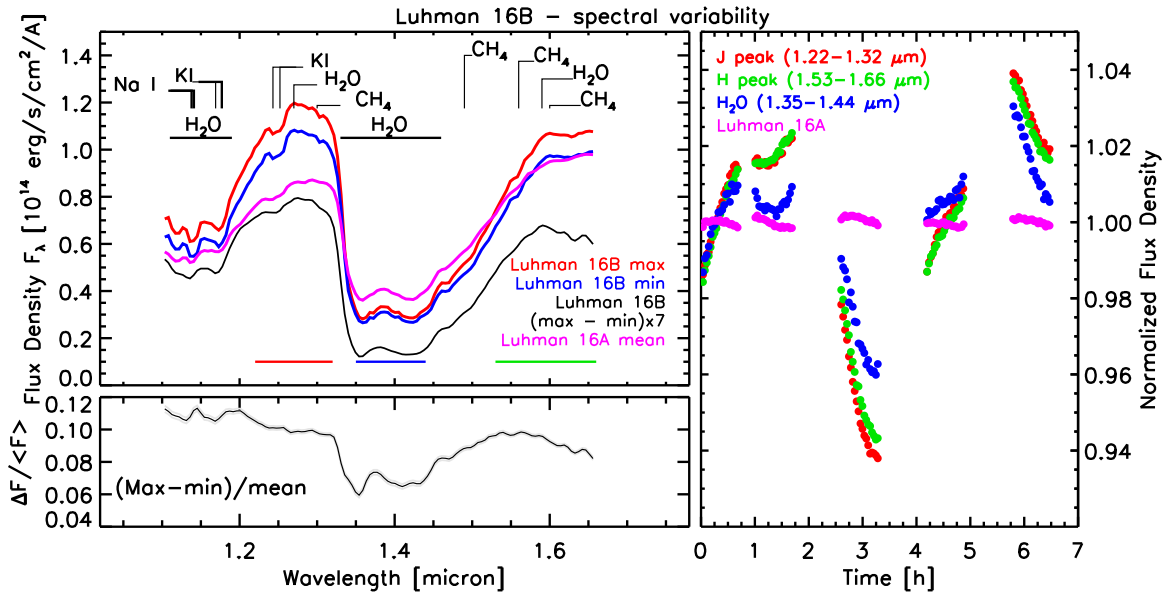
Figure 5. Observations of Luhman 16B. Top left: maximum and minimum spectrum compared to the average spectrum of Luhman 16A. The absolute variability, i.e., the difference between the maximum and minimum is also shown (scaled by a factor of seven for visibility). The colored horizontal lines indicate the wavelength range over which the spectra were integrated to derive the light curves on the right. Bottom left: relative amplitude as a function of wavelength, i.e., the difference of the maximum to the minimum divided by the mean. The 1σ error is shown as a gray band. Right: integrated light curves of Luhman 16B derived by integrating the counts in different spectral regions. The integrated light curve over the whole wavelength range for Luhman 16A is shown for comparison. The small variations correspond to systematic errors.

are very comparable between Luhman 16A and B, this error will also be of similar size. We therefore use the non-variable Luhman 16A to determine this error to avoid the intrinsic variability of Luhman 16B to overinflate our errors. Assuming that the non-Gaussian trends in the light curves of Luhman 16A appear on timescales longer than a few minutes, we calculate the standard deviation between five neighboring (unbinned) spectra and then average over all these measurements. The error in each wavelength point for each binned spectrum lies between $\approx 0.2\%$ (J and H band peaks), and 0.3% (water absorption band and blue spectrum edge). For the relative amplitude $\Delta F/\langle F\rangle$, we increased the binning and smoothed over one resolution element, the error per resolution element there lies between 0.1% and 0.2%. This error is marked by the gray band in Figure 5. The bump in the Na I line, as well as the dip at $1.63\,\mu$m appear to be real, as well as much of the structure within the water absorption band.

3.2.1. Principal Component Analysis

Analogous to the analysis done in Apai et al. (2013) we perform a PCA on the data to determine the number of independent variable components. We subtract the mean spectrum over all orbits and then calculate the components that are variable on top of the mean. We find that 93% of the variability is described by the first component. The first component and its coefficient, which is essentially identical in shape to the integrated light curve, is shown in Figure 6. We also show the second component which accounts for 2.2%. However, this component clearly corresponds to an instrumental effect as its coefficient shows small decreasing trends within each orbit similar to what was found for Luhman 16A. The spectral signature of this component shows a feature at the position of the rapid flux drop into the $1.4\,\mu$m water band and at the spectral edges. This is indicative of positional shifts in the x-direction during one orbit. All other components account for $<0.5\%$ of the variability. We can therefore reliably conclude that the spectral variability is for

the most part characterized by only two distinct photospheric structures whose visible fractional coverage varies as the brown dwarf rotates.

We reconstruct a time series using only the mean and first component spectrum, $F'(t,\lambda) = \langle F(t,\lambda)\rangle_t + a_1(t)e_1(\lambda)$ to remove some of the noise and instrumental systematics contained in higher order components. In particular, we recalculate the difference between the minimum and maximum spectrum which characterizes the wavelength-dependent amplitude changes (Figure 6, bottom left). In this case, we have used the full time series, and not only the actual maximum and minimum spectrum, to derive this wavelength dependence. This should help average out systematic uncertainties that may be particularly problematic as they are largest between the beginning and end of an orbit. Since the maximum occurs at the beginning of orbit 5 and the minimum at the end of orbit 3, these systematics may have a significant effect on the ratio shown in Figure 5. Indeed, we find that $\Delta a_1 e_1(\lambda)/\langle F\rangle$, where Δa_1 is the difference between the maximum and minimum of $a_1(t)$, is approximately 0.4% lower for most wavelengths, and 1%–1.5% in the water band, than $\Delta F/\langle F\rangle$, which was derived from only the maximum and minimum spectra. This agrees with the derived systematic uncertainties (Section 3.1.1). However, the shape of the ratio over the water band is also different, which indicates that the water varies slightly differently over the course of observations. Indeed, comparing a reconstructed light curve with only one PCA component in the water band with the original light curve reveals significant differences (Figure 7). Because the signal in the water band is much lower and the noise larger than in the other regions, this difference is hidden within a combination of higher order components in the PCA. It indicates that while a two-component model can broadly account for most of the spectral variability, additional smaller variations in the deep water band are also present. The differences are overall larger than the $\approx \pm 0.5\%$ uncertainty found in the Luhman 16A water light curve. Small differences of up to $\pm 0.3\%$ are also found for the
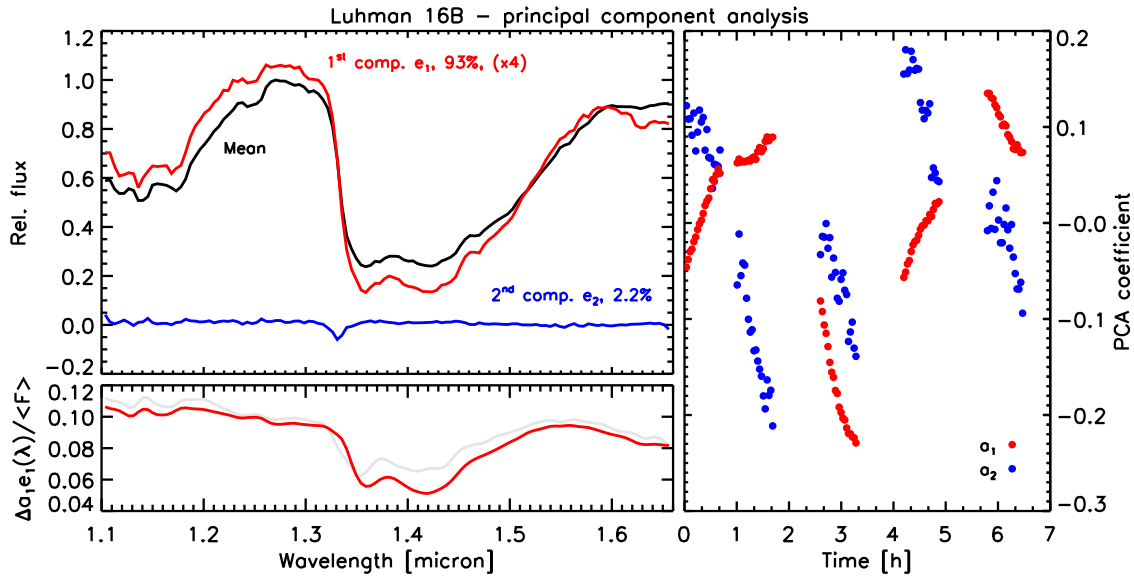
Figure 6. Principal component analysis for Luhman 16B. Top left: first (red) and second (blue) principal components compared to the mean spectrum (black). They are normalized to the maximum of the mean component. The first component is additionally scaled up by a factor of four for better visibility. Bottom left: variability amplitude (maximum difference of coefficients multiplied by the component and divided by the mean) derived from the first component (red) compared to the variability amplitude from the maximum and minimum spectrum (gray, same as in Figure 5). Right: coefficients c of the first and second components.
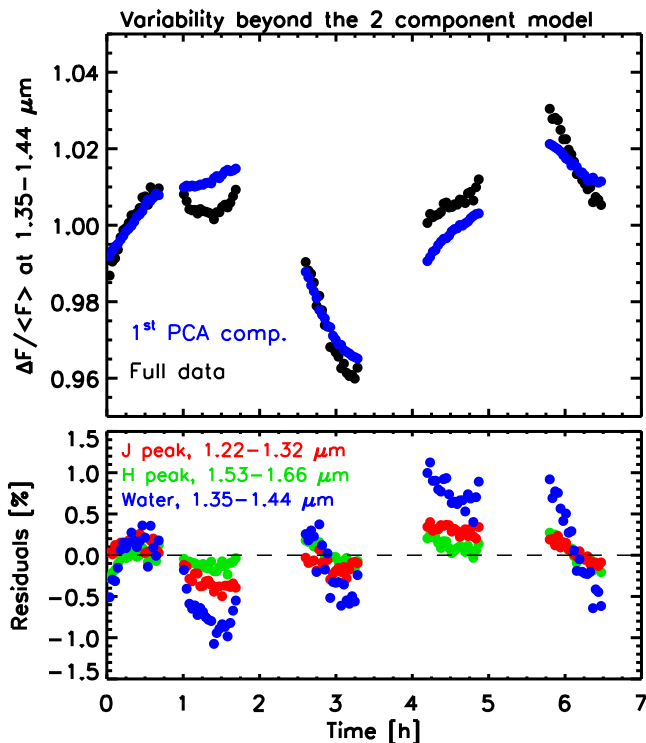

Figure 7. Top: light curves of Luhman 16B obtained from integrating the spectral time series over the water band between 1.35 and 1.44 μm. The black points were obtained from the full data cube, while the blue points were obtained from the spectra reconstructed using only the first principal component, i.e., assuming a two-component cloud model. Bottom: difference between the light curve using the full data and using only the first principal component for the water band, compared to the J band peak (red) and H band peak (green).

J band peak but it is unclear whether these deviations are of astrophysical origin.

We don't find any other significant differences in the wavelength dependence, but it is possible that in this procedure we have removed small astrophysical variations that were hidden within the higher order components that we classified as random

noise or systematic errors. However, because only two components clearly contribute to most of the variability, we will only attempt to build a two-component model (see Section 4) and therefore also only fit to the dimensionally reduced data.

3.2.2. Evolution over One Rotational Period

The rotation period of Luhman 16B has been estimated to be 4.87 ± 0.01 h by Gillon et al. (2013) and 5.05 ± 0.1 hr by Burgasser et al. (2014) based on observations spanning several days. From our observations over 6.5 hr we can therefore discuss the spectral changes that have happened over the course of one rotation. In Figure 8, we show the parts of the phase-folded light curve where we have coverage for two rotations. Clearly, the light curve has evolved significantly over only one rotation period. At the beginning of the overlap, we find a higher brightness of 1%–2% for the second rotation than for the first, and presumably an even larger difference during the gap where observations are missing for the first rotation. Also, in the first rotation, the light curve is increasing, but it is rapidly decreasing at the same phase during the second rotation.

The spectra between the two rotational phases are largely identical within the noise level (Figure 8, right), except for an offset where the brightness is different. The only difference is found within the deep water band at 1.4 μm, as well as in the absorption band shortward of 1.2 μm. In the second rotational phase there is slightly more flux ($\sim$0.5%) in the water band compared to the other wavelengths. This is interesting because from our previous analysis we would expect the relative flux in the water band to be slightly lower in the brighter rotational phase because the overall variability amplitude is lower in the water band. The fact that we find the opposite provides additional evidence that there are additional small variations present in the water band that are not captured by our PCA.

3.3. Relative Angular Distance and Position Angle

Luhman 16A and B are the only two sources with significant signals in the field of view of our 256 × 256 pixels sub-array WFC3/IR images. Therefore, we cannot obtain their positions
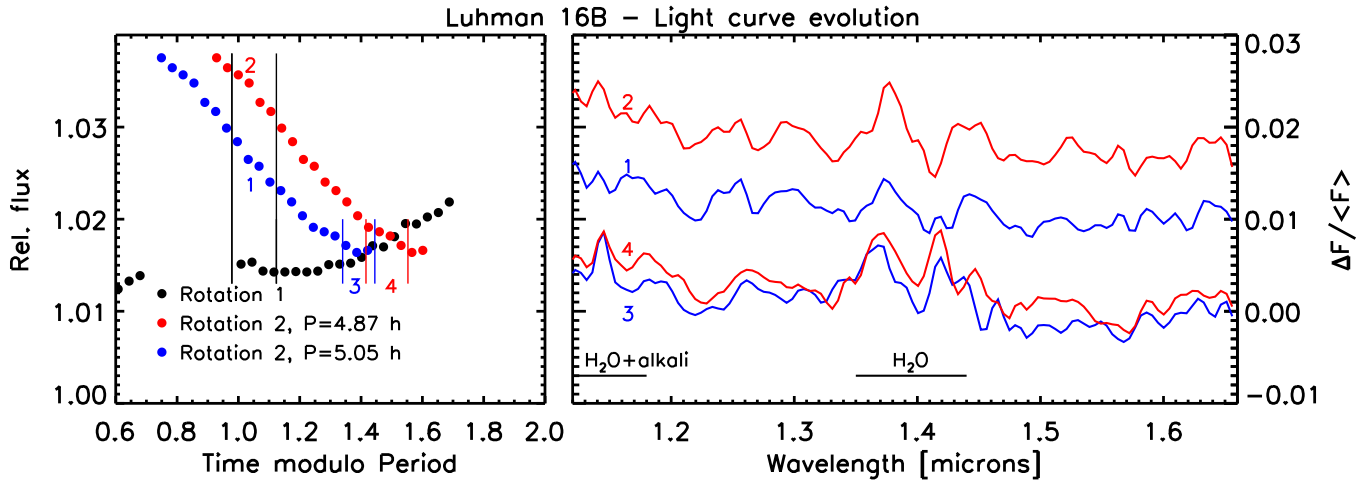
Figure 8. Light curve and spectral evolution of Luhman 16B within one rotation period. Left: part of the phase folded integrated light curve where the observations covered the same rotational phase twice. The first observation is shown in black and the second is phase folded using two possible periods (4.87 hr, red) and (5.05 hr, blue). The vertical lines with numbers indicate which part of the light curve was averaged to analyze the spectra. Right: Difference of spectra $(S2 - S1)/((S1 + S2)/2)$ where $S1$ and $S2$ denote the spectra taken in the first or second rotational phase at the positions indicated on the left plot.

with respect to "fixed" background objects. The absolute angular distance and positional angle between Luhman 16A and B will ultimately be at the mercy of the instrument calibration and characterization of its stability.

To measure the positions in individual images, we employed the PSF-fit software and library developed by Jay Anderson.[10] It is an adaptation of the program first presented in Anderson & King (2006); a small additional adaptation was done by us to read 256×256 subarray images. With only the two brown dwarfs visible, we cannot meaningfully solve for both the positions and PSF of the objects, we therefore adapted a library PSF. We used the PSF for filter F139M, which is the closest available to that of the filter F132N in which our direct images were taken. We extracted the raw pixel coordinates from the `flt` images using the `img2xym_wfc3ir` routine and corrected them for the geometric distortion with the program `wfc3ir_cg`, which uses the best available solution currently available at the Space Telescope Science Institute.

We then computed, for each of the two axes, the difference in geometric-distortion corrected positions between Luhman 16A and B. The average and scatter of their relative angular distance in pixels from our five images is $\Delta r = 10.292 \pm 0.019$ pixels. Adopting a pixel scale of 120.99 mas pixel^{-1} for the geometric distortion correction developed by Anderson, the separation of the two components of Luhman 16 amounts to 1245.2 ± 2.3 mas. The uncertainty reflects only the internal errors and likely underestimates the true errors that might cancel out in this particular data set where images were collected under (nominally) identical conditions. The WFC3/IR pixel scale is stable down to 5 parts in 10,000 (J. Anderson 2014, private communication), and it is significantly more stable than for WFC3/UVIS. Therefore we add to the above quoted uncertainty an additional error of ± 1.3 mas.

The above method is the most accurate to derive relative separations, but it is not normalized to the guide stars on which the roll angle relies. To derive the position angle, we therefore use the `drz` images output from the *HST* pipeline, which are distortion corrected and include WCS information; however, no library PSFs are available. Our five original direct images were

combined by the pipeline into two separate distortion corrected images. We measure the positions of the binary components by determining the photo-centroid. We find a position angle P.A. = $311° \pm 3°$. The dominating error component derives from the uncertainty in the photo-centroid determination. We conservatively assume 0.5 pixels error in the distances Δx and Δy between the binary. The additional uncertainty in the north direction because of the error in roll angle is less than an arcminute, and therefore negligible.

The separation of Luhman 16AB, here measured as $1\rlap{.}''25$, has clearly decreased since the epoch where its binarity was first recognized. The binary separation was given as $1\rlap{.}''5$ by Luhman (2013) from a GMOS measurement taken on 2013 February 23, although without specifying an error bar. Immediate follow-up by Burgasser et al. (2013) indicated a separation of $1\rlap{.}''54 \pm 0\rlap{.}''04$ on 2013 March 12 at a position angle of $313° \pm 3°$. Further astrometric measurements were obtained by Boffin et al. (2014) between April 14 and 2013 June 22, where the separation decreased from $\approx 1\rlap{.}''43$ to $1\rlap{.}''36$. Within eight months, the projected binary separation has therefore shrunk by approximately $0\rlap{.}''3$. The position angle has remained constant within error bars. We refrain from constraining the binary orbit because dedicated programs to obtain high-precision astrometry of the system with both *HST* and FORS2 are ongoing that will deliver much more accurate results. However, our result shows that it will be important for future observing campaigns of this binary to take into account that the separation may have further decreased and that resolving them spatially may become considerably more challenging, especially without adaptive optics from the ground.

4. ATMOSPHERE MODELING

We use models based on the Ackerman & Marley (2001) cloud models that have been updated with new opacities for H_2 collision-induced absorption (CIA), NH_3 and FeH (Saumon et al. 2012). The models parameterize the clouds with the sedimentation efficiency f_{sed}. A smaller f_{sed} value corresponds to a vertically and optically thicker cloud. Our analysis uses a grid of models covering $f_{sed} = 1, 2, 3$ and non-cloudy (nc), effective temperatures T_{eff} between 900 and 1500 K in 100 K steps, gravity $\log g = 4.5$ and 5, and the vertical mixing

---

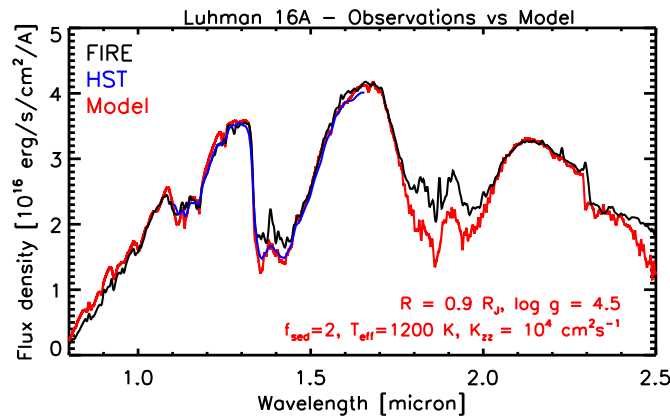[10] Available at http://www.stsci.edu/~jayander/WFC3/WFC3IR_PSFs/.

Figure 9. *HST* and FIRE spectra of Luhman 16A compared to the best-fit model. FIRE spectrum from Burgasser et al. (2013).

parameter $K_{zz} = 0$ and 10^4 cm^2 s^{-1}, which controls departures from equilibrium chemistry (see Stephens et al. 2009, for detail). Because we also fit for the absolute flux level, the radius R of the brown dwarf is an additional free parameter. We use a distance of 2.02 pc determined from the parallax by (Boffin et al. 2014).

We simultaneously try to match the overall average *HST* spectrum and the broader 0.8 –2.5 μm FIRE spectrum (from Burgasser et al. 2013), as well as the relative amplitude as a function of wavelength $\Delta F / \langle F \rangle$ for Luhman 16B. We note that the ground-based FIRE spectrum is strongly affected by telluric water lines between 1.35 and 1.45 μm and between 1.8 and 2 μm; we disregard the FIRE observations for these regions but we fit the 1.35–1.45 μm region from the *HST* spectrum.

For both Luhman 16A and B, it is obvious that models with $K_{zz} = 0$ cm^2 s^{-1} cannot properly reproduce the shape of the K band spectrum. If we allow for out-of-equilibrium chemistry by setting $K_{zz} = 10^4$ in the calculation of the synthetic spectra, the shape of the K band spectrum can be matched reasonably well. We therefore continue only with those models. We note that the calculation of vertical mixing is also not fully self-consistent because there is no feedback between the modified chemistry and the temperature-pressure profile of the atmosphere based on equilibrium chemistry.

We first model the spectrum of Luhman 16A. The only model that provides a very good fit has parameters $T_{\rm eff} = 1200$ K, $f_{\rm sed} = 2$, log $g = 4.5$, $K_{zz} = 10^4$ cm^2 s^{-1} and $R = 0.95$ $R_{\rm J}$ (Figure 9). This radius is about 20% lower than the evolution radius for these parameters (Saumon & Marley 2008).

For Luhman 16B, none of the models reproduce the average spectrum. This is unsurprising, as the variability indicates that we require more than a homogeneous cloud model. Because most of the observed spectral variability can be explained by two components, we attempt to fit a model that is a linear combination of two models with different cloud properties and effective temperatures. We note that because these two models have different temperature–pressure profiles, which would be coupled in reality, the calculations are not self-consistent. First attempts at more realistic patchy cloud models have been made by Marley et al. (2010) and Morley et al. (2014), but that modeling framework is not yet fully ready for large-scale fitting of observations. We defer such patchy cloud modeling to a future paper. Nevertheless, the linear combination models can be seen as a useful first step in constraining the parameter space of possible cloud properties.

The two models that are linearly combined can have different effective temperatures $T_{\rm eff,1}$ and $T_{\rm eff,2}$ and different cloud
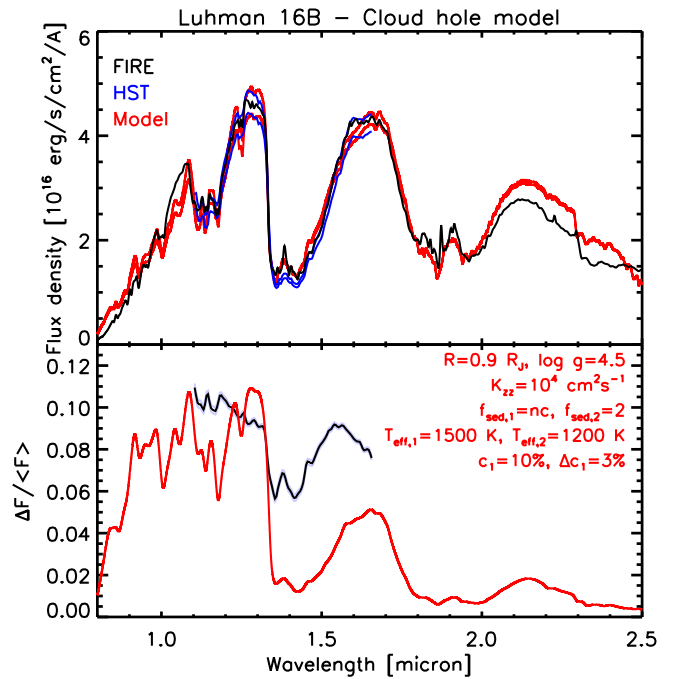

Figure 10. Top: average FIRE spectrum (black) and *HST* maximum and minimum spectra (blue) of Luhman 16B compared to a model that introduces a small fraction of hot, non-cloudy regions. Bottom: relative amplitude as a function of wavelength, i.e., the difference of the maximum to the minimum spectrum divided by the mean for the *HST* observations compared to the model. Such a model cannot reproduce the observed variability.

parameters $f_{\rm sed,1}$ and $f_{\rm sed,2}$. log g and K_{zz} have to be equal for the two models. The weights in the linear combination are set using the covering fraction c_1 of the warmer model on the hemisphere where the emitted flux is maximal, and the change in covering fraction Δc_1. Then, the combined flux $F_{\rm max} = c_1 F_1 + (1 - c_1) F_2$ and $F_{\rm min} = (c_1 - \Delta c_1) F_1 + (1 - (c_1 - \Delta c_1)) F_2$.

Because the parameter space is large and results of chi-square fitting strongly depend on the weights assigned to different spectral regions, we iteratively fit the models by eye. We only discuss approximate best fits and degeneracies, and defer a more quantitative model fitting to a later paper, once self-consistent patchy cloud models become available.

We first try cases that use the cloud model from Luhman 16A as a base ($T_{\rm eff} = 1200$ K, log $g = 4.5$, $f_{\rm sed} = 2$, $K_{zz} = 10^4$ cm^2 s^{-1}), and introducing non-cloudy areas to approximate cloud clearings. We find that the spectral shape can be approximately matched—although not perfectly in the K band—by introducing non-cloudy sections with $T_{\rm eff} = 1500$ K and covering fractions of 7%–10%. However, the wavelength dependence of the relative amplitudes induced by such cloud holes is very different than observed (Figure 10). This is unsurprising considering that similar conclusions had already been drawn about the other two known variable early-T dwarfs in Radigan et al. (2012) and Apai et al. (2013). Combinations of different cloudy and non-cloudy models do not provide better results. We can therefore exclude holes without cloud opacity as the cause of variability for Luhman 16B.

We proceed with combining models with different values of $f_{\rm sed}$. We cannot conclusively discriminate between models of different gravities, but the best-fit cloud parameters change somewhat depending on the choice of gravity. We therefore provide best-fit models for both log $g = 4.5$ and 5. These are shown in Figure 11. Regardless of log g, we find that we require a model combination of $f_{\rm sed,1} = 3$ and $f_{\rm sed,2} = 1$ and effective
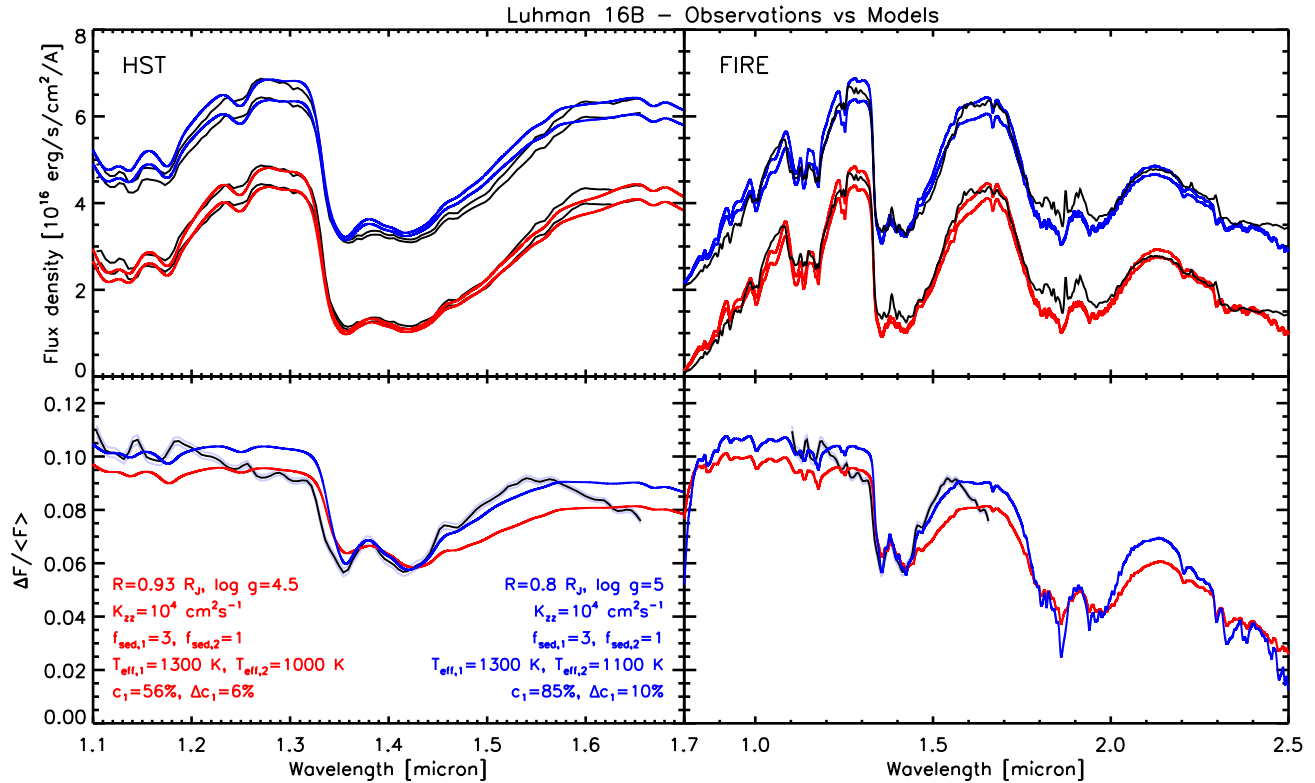
Figure 11. Modeling for Luhman 16B. Top left: *HST* maximum and minimum spectra (black) and two best-fit models with log $g = 4.5$ (red) and log $g = 5$ (blue). For clarity, observation and model for one of the cases are plotted with a vertical offset of 2×10^{16} erg/s/cm/A. Bottom left: relative amplitude as a function of wavelength, i.e., the difference of the maximum to the minimum divided by the mean. Top right: the same models compared to an average FIRE spectrum covering a wider wavelength range. Bottom right: model predictions for the relative amplitude for the extended wavelength range. The measured variability from *HST* is overplotted.

temperatures in the 1000–1400 K range, with the thinner cloud (larger f_{sed}) being warmer.

Models with other combinations of f_{sed} cannot fit the average spectrum and/or show strong deviations in the fit of the relative amplitudes. The effective temperature of the two models is degenerate with the covering fraction, but we can restrict $T_{eff,1} - T_{eff,2}$ to 200–300 K because lower and higher temperature differences fail to give the correct relative amplitude in the water band compared to the flux peaks. For both log g values, the best models have $T_{eff,1} = 1300$ K, while the cooler model has $T_{eff,2} = 1000$ K for log $g = 4.5$ and $T_{eff,2} = 1100$ K for log $g = 5$. Although we cannot fully exclude models with temperatures of 100 K higher or lower, the spectral fit tends to be worse especially in the K band.

In general, the smaller the temperature difference, and the lower the effective temperature of the warmer model, the larger the covering fraction c_1 of the warmer cloud has to be. The covering fraction of the warmer cloud can lie between $\approx 30\%$ and 90%. For our best-fit models, we find $c_1 = 56\%$ and $\Delta c_1 = 6\%$ in the case of log $g = 4.5$, but $c_1 = 85\%$ and $\Delta c_1 = 10\%$ for log $g = 5$, where Δc_1 is the change in the covering fraction of model 1 between the two hemispheres, as outline above. Derived radii are physically reasonable (0.93 R$_J$ or 0.8 R$_J$) but remain systematically lower than those corresponding to the evolution radius (Saumon & Marley 2008). We note that these results could potentially change, in particular with respect to the covering fractions, if we also allowed intermediate values for T_{eff} and/or f_{sed}, or values of f_{sed} below 1.

The overall spectral shape fits surprisingly well, although the flux in the water band and wing is overestimated in the log $g = 5$ case. On the other hand, for log $g = 4.5$ the shape of the H band peak in the FIRE spectrum is not well

fit. The main characteristics of the spectral variability are also reproduced fairly well, in particular the approximate relative amplitude in the J, water and H bands. We cannot find any model that accurately fits the slope between 1.1 and 1.3 μm, nor the wavelength dependence of the relative amplitude across the H band beyond 1.56 μm. However, the amplitude difference between the absorption bands at 1.14 and 1.4 μm and the outside continuum are approximately reproduced. The differences in the relative amplitude between model and observations are at most 2%. The prediction that the K band amplitude is significantly lower is consistent with the results in Burgasser et al. (2014).

5. DISCUSSION

The formation and growth of cloud holes through the L/T transition has been suggested as a theory to simultaneously explain the color evolution, the re-emergence of the FeH 0.9896 μm Wing–Ford band, and the occurrence of photometric variability (Ackerman & Marley 2001; Burgasser et al. 2002; Marley et al. 2010). However, recent observational results have already revealed a more complex picture: cloud holes could not explain the spectroscopic variability of 2M2139 and SIMP0136 (Apai et al. 2013; Buenzli et al. 2014), and the FeH band is equally strong in Luhman 16A and B (Faherty et al. 2014). Our spectroscopic variability observations of Luhman 16A and B strongly support these findings and show that the cloud evolution through the L/T transition is significantly more complicated than simple formation of cloud holes. Comparing the single cloud layer found for Luhman 16A with the two for Luhman 16B, our best-fit model suggests both different effective temperature and sedimentation efficiency. We can also confidently exclude full cloud-clearings, i.e., regions

without cloud opacity, although the thin patchy clouds within a background of thick clouds can still be regarded as holes in the sense that more bright flux will emerge from these regions. However, our results suggest that the whole cloud cover can be significantly different from late-L to early-T spectral type, as opposed to having a similar cloud layer that is simply broken up or thinned out at the beginning of the L/T transition. Perhaps surprisingly, we find the thick cloud component in the T dwarf to be thicker than that of the overall cloud cover on the L dwarf.

A shortcoming of our model is that the equal depth of the FeH band is not properly reproduced. For Luhman 16B, the FeH band is predicted to be deeper than for Luhman 16A, even without the opening of cloud holes. Whether this is an issue related to the FeH opacities or Fe condensation chemistry, the patchy cloud modeling which is not self-consistent, or a more fundamental shortcoming of the cloud model remains unclear.

With the effective temperature difference between the two cloud layers estimated to 200–300 K, we arrive at a difference in covering fraction of about 5–10% between the two hemispheres. The simplest explanation for the rapid light curve evolution is then that the covering fraction changes, perhaps due to rapid redistribution of the clouds. An additional 1%–2% change in the covering fraction can already alter the relative amplitude by a few percent. Periods without or with only very low variability (Gillon et al. 2013) may simply be times when the covering fraction is approximately equal at all longitudes. The additional spectral changes beyond the two-component model suggest that small alterations in the cloud structure beyond the covering fraction can also happen on short timescales, although the major characteristics of the spectroscopic variability are preserved within a single rotation. Further epochs would be required to trace larger scale changes in the cloud structure. Some intriguing differences between our measurements and multi-wavelength photometry taken at an earlier epoch are discussed below.

5.1. Comparison to Other Observations of Luhman 16

Since its discovery in 2013, Luhman 16 has been extensively monitored for time variability from the ground over a broad wavelength range with different instruments. Monitoring over 12 nights with the TRAPPIST instrument through a special $I+z$ filter (750–1100+ nm, effective wavelength 910 nm) revealed rapidly changing variability amplitudes between 2%–11% (Gillon et al. 2013). These observations did not spatially resolve the binary. Assuming that all variability stems from Luhman 16B, this would translate to effective peak-to-valley amplitudes of 4%–22%. If the amplitudes do not significantly change at wavelengths shortward of our observations, then our observed amplitudes of ∼10% would fall into an intermediate regime.

Because of the rapid changes, single filter photometry does not provide useful information on the cloud structure for this object. Simultaneous multi-color photometry was obtained with the GROND instrument by Biller et al. (2013) on two nights in six filters spanning from the optical to the near-infrared (r', i', z', J, H, K). On one night, the observations were made in the spatially unresolved mode, in the other in spatially resolved mode. The results in the near-IR from the unresolved observations agree relatively well with our observations: the peak-to-valley amplitude in the J band was found to be 14% in the J and 8% in the H band assuming all the variability stems from Luhman 16B. The $\Delta(J-H)$ color change is larger than in our observations, but we do not fully cover the H band where

we would expect the amplitude to keep decreasing. The light curve shape in the J, H, and z' bands were very similar, but interestingly, the light curves in r' and i' bands were found to be anti-correlated to J, H, and z'. We do not find any anti-correlation in our observations, but our observations do not span the wavelengths where anti-correlation was found.

The most puzzling set of observations are the spatially resolved GROND observations taken a few days after the unresolved observations. Most interestingly, no variability was found in the J band above the photometric uncertainty of 3%, while the z' and H bands showed clear variations of 9% in the z' and 13% in the H band. These observations suggest that at that moment the wavelength dependence of the amplitude was completely different than during the unresolved observations and during our *HST* observations, as well as compared to the other known variable early-T dwarfs (see Section 5.2). The different color change in $z'-H$ might be partially explained by the large uncertainty of ∼4% in the resolved GROND H band observations. However, none of our models could produce significant variability in the H and z' bands while simultaneously not having any or only very low variability in the J band. Multi-epoch multi-wavelength monitoring would be required to confirm this very unusual change in the color signature of the variability.

The GROND observations also contained the first K band photometry, which appeared to show an intermediate phase between the phase of the correlated z' and H and anti-correlated r' and i' light curves. Biller et al. (2013) suggested a similar dependence of the phase on the atmospheric pressure probed in a band as found for the mid-T dwarf 2MASSJ2228-43 (Buenzli et al. 2012). Our observations do not show any phase shifts, even though the deep water band in our observations would probe pressures lower than the r', i', and K bands. If the K band phase shift is not an artifact of instrumental systematics, the three dimensional structure of the atmosphere of Luhman 16 is likely to be changing as well.

The first spectroscopic variability study for Luhman 16B was performed by Burgasser et al. (2014) with the SPEX instrument. They obtained a 45 minute spectral time series spanning from 0.7 to 2.5 μm at a resolution of $\lambda/\Delta\lambda \approx 120$, together with TRAPPIST photometry spanning 7 hr. These observations only looked at relative changes between Luhman 16A and B, but our observations show that at least in the near-IR the assumption that any variability of Luhman 16A is negligible compared to B appears to hold. They found decreasing flux of about 10%/hr in the Y and J bands and 7%/hr in the H band. This is in very good agreement with the color variability in our observations, as well as the maximum flux decrease in our J band observations. They also found some evidence of lower variability in the water band at 1.4 μm and a continuing decrease into the K band. However, the signal-to-noise ratio in these wavelength regions makes the measured variability non-significant. Here we clearly confirm the lower relative amplitude in the 1.4 μm water absorption band, and our model fit is fully consistent with the lower amplitudes in the K band ($\approx$4%/hr).

Our *HST* observations are overall very similar in the characteristics to the SPEX variability observations, while at least one epoch of GROND multi-wavelength photometry offers a very different picture. Additional epochs of multi-wavelength observations are required to obtain a better understanding of the rapid changes occurring in the atmosphere of Luhman 16B.

Comparing our observations to the surface map derived with Doppler imaging (Crossfield et al. 2014) is difficult, because
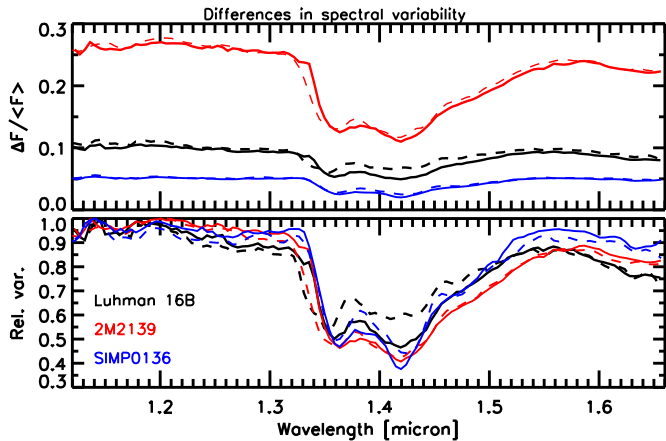
Figure 12. Wavelength dependence of the variability for Luhman 16B (black), 2M2139 (red), and SIMP0136 (blue). Top: variability amplitude as a function of wavelength calculated as the difference between the maximum and minimum spectrum divided by the mean. Bottom: the same but normalized to the maximum amplitude. The dashed lines directly use the observed maximum and minimum spectra averaged over a few minutes, the solid lines use the maximum and minimum spectra reconstructed by using only the mean and first principal component.

it is unclear how variations in the molecular line shape relate to the flux variability we observe with *HST*. Furthermore, the method of reconstruction for the surface map yields a smooth brightness distribution which does not easily translate into a two-component coverage fraction. It is possible that the largest dark spot found with Doppler imaging may correspond to the region where the coverage fraction of the thicker clouds is largest.

5.2. Comparison to Other Variable Brown Dwarfs

Luhman 16B is the fourth variable brown dwarf for which we have obtained *HST* spectroscopic time series covering one or more rotation periods after the T6.5 dwarf 2M2228-43 (Buenzli et al. 2012) and the two early-T dwarfs 2M2139 and SIMP0136 (Apai et al. 2013). Already from this very small sample a trend in variability characteristics emerged as a function of spectral type. The two early-T dwarfs showed very similar spectral dependence of the variability: the light curves were in phase at all wavelengths and with only slightly larger amplitude in the *J* than in the *H* band, but significantly lower amplitude in the deep water absorption band. The mid-T, on the other hand, showed complex phase shifts, the largest variability in the water band and a larger amplitude in the *H* than in the *J* band.

The characteristics of the spectral variability of Luhman 16 is again very similar to that of the two other early-T dwarfs: all variability is in phase (excluding the anti-correlation observed with GROND, for which we do not have similar information for the other two objects), and the water band variability is lower than in the *J* and *H* bands.

In Figure 12, we directly compare the spectral variability for the three objects both in absolute terms and scaled to the same maximum amplitude. We derived the variability difference in two ways: directly from the maximum and minimum observed spectra (averaged over a few minutes to improve the signal-to-noise ratio), as well as from the reconstructed maximum and minimum spectra using only the mean and first component from the PCA. For 2M2139 and SIMP0136 we performed a PCA exactly analogous to Luhman 16B. For 2M2139 and SIMP0136 the spectral variability is very similar in both cases, unlike for

Luhman 16B where we found a significant difference in the water band, as discussed in Section 3.2.1.

Comparing only the variability derived from the PCA, i.e., corresponding to a simple two-component model, we find that except for the different amplitudes, the spectral signature of the variability is remarkably similar for all three objects. The relative amplitude in the water band is always approximately half of the maximum relative amplitude, which is always found at 1.14 μm. All three objects also share very similar small dips at 1.12 and 1.16 μm. A small but significant difference is primarily found in the overall slope from the *J* to the *H* band: for SIMP0136, the latest type object, we find the flattest slope with only a 10% decrease from 1.2 to 1.66 μm. The slope is intermediate for 2M2139 with an 18% decrease, while the steepest slope is found for the earliest spectral type object Luhman 16B. There, the slope is already notable across the *J* band, and we find a total of 25% decrease from 1.2 to 1.66 μm. These values are consistent with the *J*−*H* variability found in different epochs for Luhman 16B (Burgasser et al. 2014) and 2M2139 (Radigan et al. 2012), although we note that for 2M2139 significant changes in the *J*−*K* color were found during nights only a few days apart.

In terms of variability amplitudes, Luhman 16B (10.5%) is here found to be intermediate between 2M2139 (27%) and SIMP0136 (5.5%), although these values are known to change significantly between epochs. Luhman 16B is also intermediate in terms of rotation period (5 hr), compared to 7.8 hr for 2M2139 and 2.4 hr for SIMP0136. This was already noted by Burgasser et al. (2014) who discuss the connection to the Rhines scale, which provides an estimate of the maximum possible feature size and scales linearly with rotation period and wind speed (see also Apai et al. 2013). For a more slowly rotating object, the occurrence of larger features are possible. At equal covering fraction, larger features would also imply fewer features, which then have a higher probability of being distributed unequally. For these three objects, the results are consistent with potentially larger features on the more slowly rotating objects. However, without good constraints on the covering fractions of the respective components, no strong conclusions can be drawn.

6. CONCLUSIONS

As our nearest brown dwarf neighbors, the Luhman 16AB system offers unprecedented opportunities to further our understanding of the L/T transition. We have obtained a very high signal-to-noise ratio, spatially resolved spectroscopic time series of both objects with *HST* that reveal a highly patchy cloud structure for Luhman 16B.

Our main conclusions are:

1. Luhman 16A is not variable at 1.1–1.66 μm above our instrumental systematics of $\approx$0.2%–0.4% depending on wavelength. A model with a single, homogeneous cloud layer with $T_{\rm eff} = 1200$ K, $f_{\rm sed} = 2$, $\log g = 4.5$ and out-of-equilibrium chemistry with $K_{zz} = 10^4$ cm^2 s^{-1} provides a good fit to the spectrum.

2. Luhman 16B varies with a maximum peak-to-peak amplitude of more than 10% in the near-IR, but the relative amplitude is lower in the deep water absorption band at 1.4 μm. Outside the absorption band there is also a small decrease in the relative amplitude with increasing wavelength.

3. A two-component cloud model can explain most, but not all, of the variability of Luhman 16B, with the primary differences seen in the water absorption band. A combination

of a warmer, thinner cloud with $T_{eff} = 1300$ K and $f_{sed} = 3$ and a cooler, thicker cloud with $T_{eff} = 1000$–1100 K and $f_{sed} = 1$ provide a decent fit to both the spectrum and relative amplitude as a function of wavelength, but the covering fraction of each cloud is degenerate with other model parameters. The relative covering fraction varies by 5%–10% between the two hemispheres. Out-of-equilibrium chemistry ($K_{zz} = 10^4$ cm^2 s^{-1}) is also required to fit the spectrum.

4. We can firmly exclude the existence of areas without cloud opacity, suggesting that the primary difference in the color and the variability between a co-eval late-L and early-T dwarf is not caused by the opening and clearing of deep holes. Instead, we find a difference in the cloud structure before the L/T transition (overall intermediate cloud thickness) to within the transition (patchy coverage with thicker and thinner clouds).

5. The relative amplitude shows very similar wavelength-dependent behavior for the three known highly variable early-T dwarfs, suggesting similar underlying cloud structure that may be typical for these objects.

6. The light curve shape and amplitude of Luhman 16B evolves significantly on the timescale of only one rotation period. Between epochs, the wavelength dependence of the variability may also change significantly, although it is unclear what mechanism could cause these changes.

7. The projected separation of Luhman 16A and B has decreased by 0.″3 within a timespan of eight months.

Further monitoring of the orbital evolution with *HST* (Program #13748), *Gaia*, and from the ground will eventually result in a dynamical mass measurement, a crucial input for the constraint of atmospheric models. Combined with continuing monitoring of the variability of Luhman 16B across a wide wavelength range and the direct comparison to its companion Luhman 16A, it will be possible to put together a comprehensive model of its atmosphere and weather patterns that cannot be obtained for any other substellar object.

REFERENCES

Ackerman, A. S., & Marley, M. S. 2001, ApJ, 556, 872
Anderson, J., & King, I. R. 2006, Instrument Science Report ACS 2006-01, 34 pages, 1
Apai, D., Radigan, J., Buenzli, E., et al. 2013, ApJ, 768, 121
Artigau, É., Bouchard, S., Doyon, R., & Lafrenière, D. 2009, ApJ, 701, 1534
Biller, B. A., Crossfield, I. J. M., Mancini, L., et al. 2013, ApJL, 778, L10
Boffin, H. M. J., Pourbaix, D., Mužić, K., et al. 2014, A&A, 561, L4
Buenzli, E., Apai, D., Morley, C. V., et al. 2012, ApJL, 760, L31
Buenzli, E., Apai, D., Radigan, J., Reid, I. N., & Flateau, D. 2014, ApJ, 782, 77
Buenzli, E., Marley, M. S., Apai, D., & Lupu, R. E. 2014, arXiv:1406.0210
Burgasser, A. J., Gillon, M., Faherty, J. K., et al. 2014, ApJ, 785, 48
Burgasser, A. J., Kirkpatrick, J. D., Liebert, J., & Burrows, A. 2003, ApJ, 594, 510
Burgasser, A. J., Marley, M. S., Ackerman, A. S., et al. 2002, ApJL, 571, L151
Burgasser, A. J., Sheppard, S. S., & Luhman, K. L. 2013, ApJ, 772, 129
Burrows, A., Sudarsky, D., & Hubeny, I. 2006, ApJ, 640, 1063
Crossfield, I. J. M., Biller, B., Schlieder, J. E., et al. 2014, Natur, 505, 654
Cushing, M. C., Marley, M. S., Saumon, D., et al. 2008, ApJ, 678, 1372
Dupuy, T. J., & Liu, M. C. 2012, ApJS, 201, 19
Faherty, J. K., Beletsky, Y., Burgasser, A. J., et al. 2014, ApJ, 790, 90
Gillon, M., Triaud, A. H. M. J., Jehin, E., et al. 2013, A&A, 555, L5
Kirkpatrick, J. D. 2005, ARA&A, 43, 195
Knapp, G. R., Leggett, S. K., Fan, X., et al. 2004, AJ, 127, 3553
Kniazev, A. Y., Vaisanen, P., Mužić, K., et al. 2013, ApJ, 770, 124
Kuntschner, H., Kümmel, M., Walsh, J. R., & Bushouse, H. 2011, ST-ECF Instrument Science Report WFC3-2011-05, 5
Luhman, K. L. 2013, ApJL, 767, L1
Mandell, A. M., Haynes, K., Sinukoff, E., et al. 2013, ApJ, 779, 128
Marley, M. S., Saumon, D., & Goldblatt, C. 2010, ApJL, 723, L117
Morley, C. V., Marley, M. S., Fortney, J. J., & Lupu, R. 2014, ApJL, 789, L14
Swain, M., Deroo, P., Tinetti, G., et al. 2013, Icar, 225, 432
Radigan, J., Jayawardhana, R., Lafrenière, D., et al. 2012, ApJ, 750, 105
Radigan, J., Lafrenière, D., Jayawardhana, R., & Artigau, E. 2014, ApJ, 793, 75
Saumon, D., & Marley, M. S. 2008, ApJ, 689, 1327
Saumon, D., Marley, M. S., Abel, M., Frommhold, L., & Freedman, R. S. 2012, ApJ, 750, 74
Stephens, D. C., Leggett, S. K., Cushing, M. C., et al. 2009, ApJ, 702, 154
Tsuji, T., Nakajima, T., & Yanagisawa, K. 2004, ApJ, 607, 511